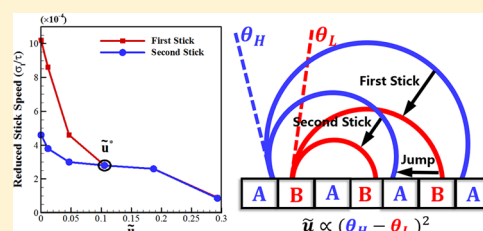


Pinning–Depinning Mechanism of the Contact Line during Evaporation of Nanodroplets on Heated Heterogeneous Surfaces: A Molecular Dynamics Simulation

Jiajian Zhang, Haibo Huang,* and Xi-Yun Lu

Department of Modern Mechanics, University of Science and Technology of China, 96 JinZhai Road, Hefei 230026, Anhui, China

ABSTRACT: Droplet evaporation on heterogeneous or patterned surfaces has numerous potential applications, for example, inkjet printing. The effect of surface heterogeneities on the evaporation of a nanometer-sized cylindrical droplet on a solid surface is studied using molecular dynamics simulations of Lennard-Jones particles. Different heterogeneities of the surface were achieved through alternating stripes of equal width but two chemical types, which lead to different contact angles. The evaporation induced by the heated substrate instead of the isothermal evaporation is investigated. It is found that the whole evaporation process is generally dominated by the nonuniform evaporation effect. However, at the initial moment, the volume expansion and local evaporation effects play important roles. From the nanoscale point of view, the slow movement of the contact line during the pinning process is observed, which is different from the macroscopic stationary pinning. Particularly, we found that the speed of the contact line may be not only affected by the intrinsic energy barrier between the two adjacent stripes (\tilde{u}) but also relevant to the evaporation rate. Generally speaking, the larger the intrinsic energy barrier, the slower the movement of the contact line. At the specified temperature, when \tilde{u} is less than a critical energy barrier (\tilde{u}^*), the speed of the contact line would increase with the evaporate rate. When $\tilde{u} > \tilde{u}^*$, the speed of the contact line is determined only by \tilde{u} and no longer affected by the evaporation rate at different stages (the first stick and the second stick).



INTRODUCTION

Droplet evaporation on heterogeneous or patterned surfaces may be observed in numerous applications such as inkjet printing,¹ DNA stretching and DNA mapping,^{2,3} coating,⁴ and nanopatterning.⁵ Understanding the inherent mechanism of droplet evaporation on heterogeneous surfaces is helpful to design functional patterns and produce smart devices.

A significant amount of experimental and theoretical work has been carried out to understand the behavior or mechanism of droplet evaporation. Some studies focused on how the contact line and contact angle change during evaporation, whereas some highlighted factors influencing the evaporation rate.^{6–21} The first theory of the evaporation of a free droplet surrounded by gas has been proposed by Maxwell about 100 years ago.²² Since then, relevant theories have been further developed and refined. For instance, based on the dynamics of the contact line and contact angle, three different evaporation modes have been proposed: the constant contact radius (CCR) mode,^{6,11,19} the constant contact angle (CCA) mode,^{9,11,16,19} and the mixed mode.^{11,15,19} In the CCR mode, the contact line is pinned and immobilized on the solid substrate and contact area remains constant, which result in a diminishing contact angle during evaporation. In the CCA mode, the contact line keeps on receding toward the center of the droplet, whereas the contact angle remains unchanged. In the mixed mode, both the contact line length and contact angle change during evaporation, which usually takes place at the end of evaporation.

The dynamics of the contact line and contact angle may be found more complicated due to the surface morphology and chemical composition.^{23–40} The first molecular dynamics (MD) simulations for the evaporation of nanodroplets on chemically stripe-patterned surfaces under a constant-temperature condition were carried out by Wang and Wu.³⁵ The evaporation was achieved by extracting the liquid molecules from the droplet surface; in other words, the evaporation rate was a specified constant in their simulations. The pinning–depinning phenomenon (CCR–CCA transition) was observed during the evaporation with different surface morphologies. Xu et al.¹¹ experimentally studied the evaporation of sessile water droplets on micropillared superhydrophobic surfaces. It was found that with the decrease in the solid fraction the CCR mode is shortened and the CCA mode is lengthened.

There are always concerns about critical factors that result in the transition from CCR to CCA mode during the evaporation. In recent years, pinning and depinning forces^{19,41} or the energy barrier^{17,18,42} has been discussed widely to interpret evaporation behavior and the contact line motion. For example, Orejon et al.¹⁷ investigated the dynamics of the three-phase contact line of evaporating droplets on different surfaces with varying substrate hydrophobicities. According to their opinion, the depinning of the contact line on rough surfaces occurs when the intrinsic energy barrier due to surface roughness can be overcome. Chen

Received: March 18, 2019

Published: April 22, 2019

et al.¹⁹ studied the contact line dynamics during droplet evaporation on microstructured surfaces. In their work, the pinning force F_p and the depinning force F_d were formulated and it was claimed that pinning is caused by $F_p > F_d$. However, these two explanations originated from a macroscale experiment and a microscale picture of pinning is still necessary for a better understanding.

Recently, based on the MD simulations, Zhang et al.⁴³ proposed a nanoscale explanation for pinning during evaporation, i.e., the pinning should be interpreted as a drastic slowdown of the contact line dynamics during the transition between two contact angle boundaries. However, in the pinning–depinning mechanism, the stick speed and the factors that would influence the speed are still not very clear. Besides, in the study of Zhang et al.,⁴³ the evaporation was also realized by removing molecules from the system at a given rate instead of specifying a heated substrate. In this work, the MD simulations for droplet evaporation on chemically stripe-patterned surfaces were carried out, and in our simulations, the substrate was heated. We particularly focused on pinning–depinning behavior of evaporation and the thermal effect due to the heated substrate. First, the thermal effect will be discussed comprehensively. Second, from the point of view of atomic-scale interactions, it is found that the stick speed is not only related to the intrinsic energy barrier but also related to the evaporation rate.

In our simulations, for convenience, a cylindrical droplet was used in our simulations. The heterogeneity of the surface was modeled through alternating stripes of equal width of two types. In **Numerical Methods**, the details about the model and methods used in our simulations are presented. In **Results and Discussion**, the wetting properties, evaporation patterns, thermal effects, stick speed, and pinning mechanism will be discussed. Finally, in **Summary and Conclusions**, the concluding remarks are presented.

NUMERICAL METHODS

The simulation setup for evaporation of a nanometer-sized cylindrical droplet on a heated substrate is shown in **Figure 1**. There are three

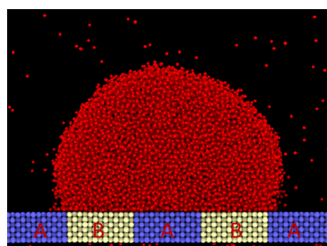


Figure 1. Schematic diagram of a cylindrical droplet on a substrate with alternating A (high equilibrium contact angle θ_A) and B (low equilibrium contact angle θ_B) stripes. The thermostat was applied to the substrate atoms to mimic the heating process. Periodic boundary conditions are applied to all three directions.

phases in the systems, i.e., the liquid droplet surrounded by its gas and the solid substrate. Lennard-Jones atoms with the parameters of argon were used to model the fluid phase because this atomic fluid has been extensively studied both experimentally and theoretically. To simplify the system, Lennard-Jones atoms were employed to model the solid substrate. The total number of argon atoms for the liquid and gas phases was 11115. Initially, these atoms were distributed on a cubic lattice with a density close to the liquid density. The solid substrate was modeled as an fcc lattice containing six layers of 1064 atoms each. The solid

substrate was placed at the bottom of the computational domain under the cubic lattice containing the liquid atoms.

The 12-6 Lennard-Jones potential [$U(r_{ij})$] was used to model the interactions between the atoms in the systems⁴³

$$U(r_{ij}) = 4\epsilon \left[\left(\frac{\sigma}{r_{ij}} \right)^{12} - \left(\frac{\sigma}{r_{ij}} \right)^6 \right] \quad (1)$$

Most parameters in Zhang et al.⁴³ were adopted here. The liquid–liquid interaction parameters were $\sigma_l = 0.3405$ nm and $\epsilon_l = 0.992$ kJ/mol, and the solid–solid interactions parameters were $\sigma_s = 0.4085$ nm and $\epsilon_s = 9.92$ kJ/mol. The mass of the liquid atoms was $m = 6.63 \times 10^{-26}$ kg. The solid atoms were 10 times heavier than the liquid ones. The temperature of the liquid and gas was $T = 119.8$ K, and its normalized value was $T^* = k_B T / \epsilon_l = 1$. The fluid property is close to that of Ar. The time unit was $\tau = (m\sigma^2/\epsilon)^{1/2}$.

Besides the fluid parameters, we have to specify the energy parameters for the fluid–solid interaction. In the following descriptions, all quantities are given in reduced units with respect to the Lennard-Jones parameters for the liquid particles. It is noted in our descriptions, if the energy parameter for fluid–solid interaction was $\epsilon_{sl}^* = n \times 10^{-1}$, the interaction strength was named “En”, where n is an integer. Because the substrate consists of stripes A and B with equal width (**Figure 1**), the fluid–solid interaction strength for the neighboring two stripes may be different. Here, when we discuss the evaporation pattern and thermal effect, the fluid–solid A and fluid–solid B interactions ϵ_{sl}^* were specified to be 0.4 and 0.7, respectively. In other words, the interaction strengths are E4 and E7, respectively. In this way, a wetting contrast between the neighboring stripes was achieved. Furthermore, the solid–liquid distance parameter was $\epsilon_{sl}^* = 1.1$. From our results, the equilibrium contact angles for E4 and E7 are $\theta_A = 119^\circ$ (hydrophobic) and $\theta_B = 79^\circ$ (hydrophilic), respectively at $T^* = 0.67$.

In our simulation, the NVT ensemble was used, where the Berendsen thermostat was chosen to control the temperature with a coupling time of 0.25τ . Note that the thermostat was applied only to the substrate atoms to mimic the heating process. The dimensions of the computational domain in the x , y , and z directions were $144.4\sigma_l$, $13.3\sigma_l$, and $283.2\sigma_l$, respectively, where z is the surface normal. Periodic boundary conditions in the three directions of space were applied in all simulations. The simulations were carried out using LAMMPS.⁴⁴ The time step and the cutoff were set to be 0.0025τ and $4.4\sigma_l$, respectively.

Initially, in the computational domain, there was no gas phase in the computational domain and all fluid particles were placed on a cubic lattice with a density close to the liquid density. At the beginning, the temperature of the whole system, including the substrate, was $T^* = 0.67$. The system relaxed to its equilibrium state where a droplet surrounded by a vapor phase was formed and the temperature everywhere was the initial T^* . Furthermore, at the equilibrium state, the droplet size no longer changed. The relaxation stage typically took about $12\,500\tau$. After the system reached the equilibrium state, the droplet was heated by suddenly increasing the temperature of the substrate to $T^* = 0.91$, yielding droplet evaporation. Besides during this process, at least 15 million time steps ($37\,500\tau$) were performed to collect enough data for further analysis of the evaporation properties. The size of the droplet and its variation upon evaporation were obtained by means of a cluster analysis. Two atoms were considered to be part of the same cluster if the distance between them was smaller than $1.5\sigma_l$.

In our simulations, the stripe width effect on evaporation was investigated. The width of each stripe was set to $1.9\sigma_l$, $6.65\sigma_l$, $11.4\sigma_l$, and $24.7\sigma_l$. The corresponding systems are named d2, d6, d12, and d24, respectively. For the d12 and d24 systems, our results show that there is not only the CCR but also the CCA mode. For the d2 system, there is only the CCA mode. These results are consistent with those in ref 43. However, in this article, we particularly focused on pinning–depinning behavior of evaporation. In the d6 system, there is only the CCR mode and it includes pinning–depinning behaviors. Hence, the results of the d6 system are taken as examples in our analysis.

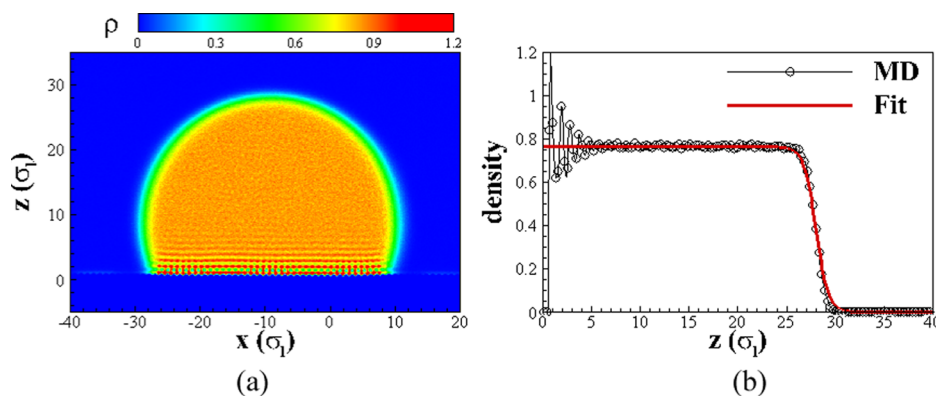


Figure 2. (a) Density contour of the equilibrium droplet, (b) mass–density along $x = -10\sigma_1$, which passes through the center of the cylindrical droplet, as a function of z . The empty circles denote the simulation data. The red solid line represents the data fitting. The system is d6 at $T^* = 0.67$.

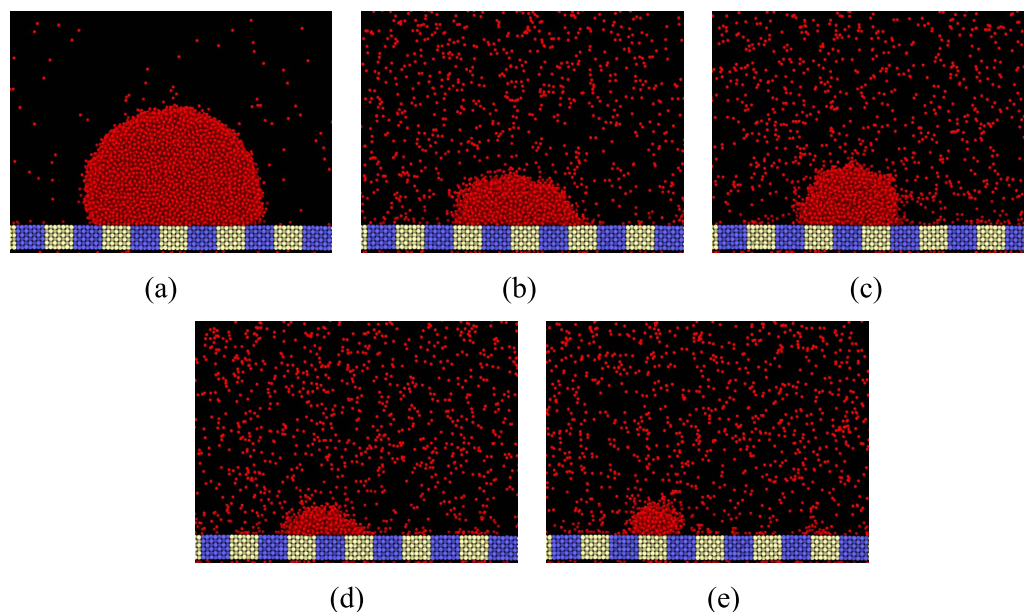


Figure 3. (a) Snapshots of the droplet evolution during the evaporation at a substrate temperature $T^* = 0.91$ for system d6: (a) $t = 0\tau$, (b) $t = 13\,750\tau$ (jump), (c) $t = 14\,500\tau$, (d) $t = 26\,500\tau$ (jump), and (e) $t = 27\,000\tau$.

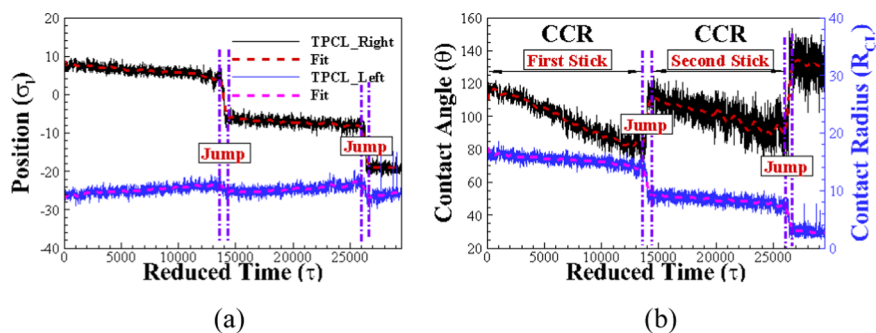


Figure 4. Quantity analysis for droplet evolution in the d6 system (substrate temperature $T^* = 0.91$). (a) Locations of the right TPCL (black line) and left TPCL (blue line) during the evaporation. (b) Contact angle θ (black line) and contact line radius R_{CL} (blue line) as functions of time. The beginning and end of the “jump” phase are denoted by the two vertical dash-dotted purple lines. All of the other dashed lines are the data fitting curves.

RESULTS AND DISCUSSION

Density in Equilibrium State. First, we would like to validate our simulations. A simulation of a d6 system at a constant temperature $T^* = 0.67$ (without heating) was performed. In the isothermal case, the initial condition is mentioned at the end of the above section. At the equilibrium

state, the droplet is surrounded by the vapor phase and the droplet volume becomes constant. The density contour of the equilibrium droplet and the mass–density distribution along $x = -10\sigma_1$, which passes through the center of the cylindrical droplet, are shown in Figure 2a,b, respectively. We suppose that the droplet is a cap of a perfect cylinder, then the location of the

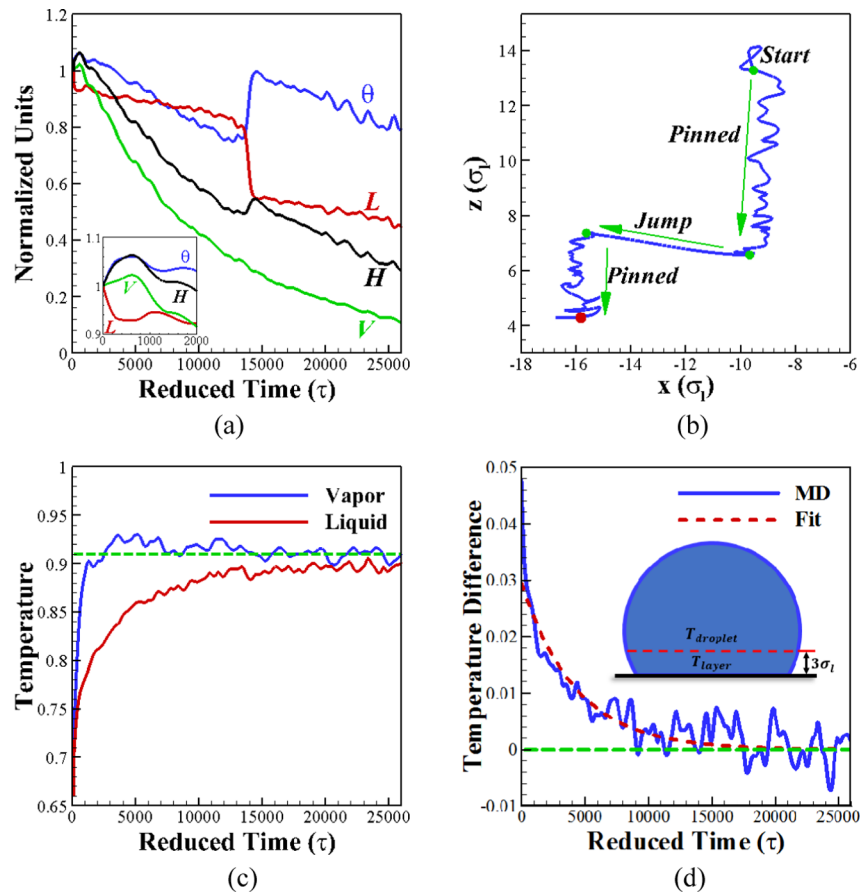


Figure 5. Geometry evolution of the droplet and temperature differences as functions of time in the d6 system with substrate's temperature $T^* = 0.91$. (a) Normalized volume V (green), base diameter L (red), droplet height H (black), and contact angle θ (blue) as functions of time. For comparison, all parameters have been normalized by their initial quantities. The curves are truncated at $26\,000\tau$ because after that moment, only a small amount of residue was left on the substrate. The inset shows the zoom-in view for $t < 2000\tau$. (b) Location of the droplet's mass center in the (x,z) -plane during the evaporation. The red point denotes the moment of truncation. (c) Average temperature evolution of the vapor and liquid phase. The green long-dash line indicates the substrate temperature $T^* = 0.91$. (d) Reduced temperature difference ($\Delta T = T_{\text{layer}} - T_{\text{droplet}}$) between the average temperature of the "absorbed" layer with a thickness of $3\sigma_l$ in the base of the droplet and the average temperature of the rest of the droplet (shown as the inset figure) as a function of time. The blue solid line and red dash line represent the simulation data and the data fitting. The green long-dash line denotes $\Delta T = 0$.

cylinder's center can be obtained from fitting the droplet isodensity contour by a circle. It is seen from Figure 2b that there are large fluctuations of mass–density distribution in the liquid near the liquid–solid interface.

The fluctuations are attributed to the strong interaction between the solid and liquid atoms that are close to the solid. The result is consistent with the observations in ref 15. It is also seen that the density distribution becomes much smoother when $z \approx 5.0\sigma_l$. The mass density decreases sharply at $z \approx 26.0\sigma_l$, indicating the location of the liquid–vapor interface. Through data fitting, we obtained a hyperbolic tangent curve

$$\rho = \frac{1}{2}(\rho_l + \rho_g) - \frac{1}{2}(\rho_l - \rho_g) \tanh\left[\frac{2(z - z_0)}{d_s}\right] \quad (2)$$

where ρ_l and ρ_g are liquid and vapor mass densities, respectively. $z_0 = 28.0\sigma_l$ is the height of the droplet, and the obtained liquid–vapor interface thickness is $d_s = 2.5\sigma_l$. It is seen that excluding the points of $z < 5.0\sigma_l$ the fitted curve agrees well with the data.

Evaporation Pattern. In this section, the simulations for systems d6 with the heated substrates were performed. The setup has been mentioned in section "Numerical Methods". The evolution of the droplet during the evaporation is shown in Figure 3, and the locations of the right and left three-phase

contact line (TPCL) during the evaporation are shown in Figure 4a. From Figure 3a, it is seen that the contact lines sit on hydrophobic stripes A. At the beginning, due to evaporation, the contact lines first move toward each other gradually ($t < 13\,600\tau$ in Figure 4a) and then cross the A \rightarrow B boundary. When $t \approx 13\,750\tau$, the droplet suddenly shifts to the left (see Figures 3b and 4a). In a short period ($13\,750\tau < t < 14\,500\tau$), the left and right contact lines both move left and quickly cross the B \rightarrow A boundary. At $t \approx 14\,500\tau$, both contact lines are close to the AB boundaries (see Figure 3c). Later ($14\,500\tau < t < 27\,000\tau$), the above process is repeated again and finally the droplet completely evaporates in a stripe B.

To quantify the evolution of the droplet during the evaporation, the contact angle (θ) and the contact line radius (R_{CL}) as a function of time are shown in Figure 4b. It is seen that according to the variation features of θ and R_{CL} there are four distinct sequential phases during the evaporation, i.e., first stick, first jump, second stick, and second jump phases. At the beginning of the first phase, both left and right contact lines interact with the AB boundaries. It is seen from Figure 4b that in the first phase the evaporation of the droplet almost follows the CCR mode because R_{CL} almost remains constant. In this stage, θ continuously decreases from $\theta \approx \theta_A$ to $\theta \approx \theta_B$. It can be understood as follows. At the beginning of the stage, we have $\theta \approx$

θ_A because the contact lines sit on hydrophobic stripe A and interact with the A stripes. While the contact radius almost remains constant as a result of the pinned contact lines, the contact angle would decrease due to the continuous evaporation. It is also seen that there is a slight decrease of the contact radius when the contact angle decreases from $\theta \approx \theta_A$ to $\theta \approx \theta_B$. From Figure 4a, it is seen that the corresponding time rate of change of the contact radius is very small but almost linear. Finally, after the contact lines cross the A \rightarrow B boundaries, the contact lines are all located in the B stripe and $\theta \approx \theta_B$. The speed of the TPCL is so small that the movement is usually neglected. Hence, the contact lines are described as pinning at the AB boundaries, and this phase is called the first stick phase. In the following section “Stick Speed and Pinning Mechanism”, we will derive a formula to describe the contact line dynamics during the stick phases.

In the second phase, which is called jump, R_{CL} and θ suddenly decrease and increase, respectively. At $t \approx 13\,600\tau$, the droplet cannot maintain the existing shape as the evaporation continues due to the depinning force¹⁹ and it would jump to its next equilibrium position. In this stage, θ quickly increases from $\theta \approx \theta_B$ to $\theta \approx \theta_A$. It is noted that θ in the jump phase presented in Figure 4b is the average value of the left and right contact angles. Later, the “stick–jump” process is repeated again. After the second jump ($t \approx 27\,000\tau$), θ is larger than θ_A . This can be attributed to the significant small droplet. First, for a very small droplet, the interfacial tensions are expected to become different and the use of Young’s contact angle equation is questionable. Second, the calculation error of the contact angle may be amplified when the volume of the droplet is small.

Thermal Effect. In this section, the thermal influence on the droplet evaporation is discussed in detail. The thermal influence due to the temperature difference between the substrate and the droplet may be decomposed into three factors, i.e., volume expansion, local evaporation near the three-phase contact line, and nonuniform evaporation across the liquid–vapor interface. The volume expansion is due to the temperature rise of the droplet. The local evaporation refers to the fast evaporation near the three-phase contact line caused by the local high temperature near the base of the droplet. Also, the nonuniform evaporation across the liquid–vapor interface is mainly caused by the unsaturated vapor pressure.

Here, we will elucidate the competition of the three factors. The geometry evolution of the droplet and temperature differences as functions of time are shown in Figure 5. From the inset in Figure 5a, it is seen that when $t < 660\tau$ the contact angle θ , droplet volume V , and the height H increase rapidly with time, whereas the base diameter L decreases rapidly. It is noted that the substrate temperature is set to be $T^* = 0.91$ at $t = 0$, which is significantly larger than the environmental temperature $T^* = 0.67$. Hence, there is a large heat flux transported from the substrate to the droplet when $t < 660\tau$, which leads to the rapid rise of the droplet’s average temperature as shown in Figure 5c. The volume expansion is dominant at this stage, which would result in the increase of V and H . However, meanwhile L decreases at first and then almost keep constant at this stage. In this way, θ increases at the stage.

The variation of L at $t < 660\tau$ can be understood as follows. In the stage, when T^* of the substrate suddenly increases from 0.67 to 0.91, there may be a temperature gradient along the z direction. Here, $\Delta T = T_{\text{layer}} - T_{\text{droplet}}$ is used to quantify the temperature difference between different parts of the droplet. Specifically, T_{layer} is the average temperature of the absorbed

layer, which is the closest layer to the substrate with a thickness of $3\sigma_v$, and T_{droplet} is the average temperature of the rest of the droplet. The evolution of ΔT is shown in Figure 5d. From the figure, we can see that there is a peak with $\Delta T \approx 0.05$ at the initial moment. On the one hand, the volume expansion makes L increase. On the other hand, the atoms with higher kinetic energy would evaporate with higher probability from the liquid–vapor interfacial region. Therefore, the evaporation close to the three-phase contact line is faster than that in another region at $T < 660\tau$. In this way, the local evaporation will make L decrease. Hence, the effects of the volume expansion and local evaporation on L are opposite. At $t < 340\tau$, the local evaporation effect may be stronger than the volume expansion effect and the base diameter shrinks slightly. At $340\tau < t < 660\tau$, the local evaporation effect is weakened and the expansion effect is enhanced. During this period, the two effects are balanced and approximately L is constant. At $660\tau < t < 1100\tau$, the expansion effect may be more significant than the local evaporation effect. L increases a little bit, but it is smaller than the initial length L_0 . In other words, the variation of L is the competition result of the volume expansion effect and the local evaporation effect.

Figure 5c,d shows that when $t > 1100\tau$ the droplet temperature reaches $T^* \approx 0.8$ and $\Delta T < 0.02$. Thus, the effects of the volume expansion and local evaporation diminish gradually. However, due to the nonuniform evaporation, V , H , L , and θ all decrease rapidly (see $1100\tau < t < 13\,600\tau$ in Figure 5a). When the contact angle decreases to θ_B at $t \approx 13\,600\tau$, the contact line is depinned and the base diameter “jumps” from $L \approx 0.8$ to 0.55, which yields an increasing θ and H at the moment. It is noticed that after jumping $\theta \approx \theta_A$ is almost achieved.

Figure 5b shows the location of the droplet’s mass center in the (x,z) -plane during the evaporation. In the pinning process ($t < 13\,600\tau$), the horizontal location of the droplet’s mass center substantially remains unchanged but the vertical location decreases rapidly, except at the initial stage ($t < 660\tau$). At the initial stage, the droplet’s mass center would slightly rise because H increases a little bit at $t < 660\tau$ (see Figure 5a). In the jump process, the height of the droplet’s mass center will increase slightly and the horizontal jump distance is approximately equal to the stripe width $6.65\sigma_1$.

From the above analysis, we found that the whole evaporation process is generally dominated by the nonuniform evaporation effect and the time span of the effect reaches $10^4\tau$. The volume expansion and local evaporation effects only play important roles at the initial moment. Also, the time span of their impact is 1 to 2 orders of magnitude lower than that of the nonuniform evaporation effect.

Stick Speed and Pinning Mechanism. In our research, we are particularly concerned about the pinning phenomenon. As we know, in the CCR mode, θ decreases with time, whereas L or R_{CL} remains constant due to the pinned contact line. In contrast to the usual CCR mode, the result in ref 43 has shown that pinning should be interpreted as a drastic slowdown of the contact line dynamics rather than a complete immobilization of it during a transition between two contact angle boundaries at the nanoscale. Our result also confirmed this point.

In this section, we will focus on stick speed in the stick–jump evaporation mode in the d6 system at the nanoscale. Here, the stick speed is quantified to describe how slow the contact line moves in the stick process. The intrinsic energy barrier would be used to quantify the constraint degree of pinning in the jump process. Therefore, the stick–jump evaporation mode links the movement of the contact line and the pinning phenomenon.

The schematic diagram of the stick–jump evaporation mode is shown in Figure 6. Initially, the base diameter and contact angle

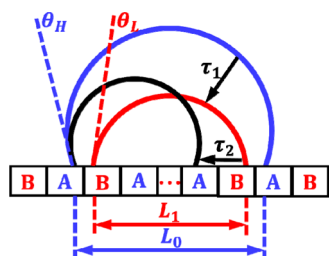


Figure 6. Schematic diagram for the stick–jump evaporation mode. A droplet on a hydrophobic surface with initial base diameter L_0 and contact angle $\theta_H = \theta_A$ evaporates in the CCR mode during time interval τ_1 . When the contact angle reaches $\theta_L = \theta_B$ and the base diameter becomes L_1 , the droplet jumps to retrieve θ_H (the black semicircle). A jump during time interval τ_2 is much shorter than that during τ_1 . This process is repeated with evaporation in the CCR mode until the droplet completely evaporates in a stripe B. $d_s = L_0 - L_1$: stick distance, $\delta\theta = \theta_H - \theta_L$: hysteresis contact angle.

of the droplet are L_0 and θ_H ($\theta_H = \theta_A$), respectively. During the time interval τ_1 , the contact lines move slowly with a stick distance d_s , and the droplet evaporates in the CCR mode until the contact angle reaches θ_L ($\theta_L = \theta_B$). In the next time interval τ_2 , the droplet jumps to a new geometry with contact angle θ_H . This stick–jump process is repeated until the droplet completely evaporates in a stripe B. In this stick–jump mode, we can see that the contact line moves with a stick distance d_s during the odd time interval τ_{odd} (i.e., τ_1, τ_3, \dots) and meanwhile there is a contact angle change $\delta\theta = \theta_H - \theta_L$, which is referred to as hysteresis contact angle. In this part, we will study the stick speed ($u_s = d_s/\tau_{\text{odd}}$) and the time rate of change of contact angle ($\delta\theta/\tau_{\text{odd}}$) in the evaporation process.

If the contact line is pinned during evaporation, the contact angle would increasingly deviate from the equilibrium value, resulting in an excess Gibbs free energy. Shanahan⁴² presented a theory in which the pinning of the contact line is modeled as an energy barrier. In this section, the theory is applied to the situation of a two-dimensional cylindrical drop. We start from

expressions for the droplet volume V , the liquid/vapor interfacial area A_{LV} , and the liquid/solid interfacial area A_{SL}

$$V = \left(\frac{\theta}{\sin^2 \theta} - \frac{\cos \theta}{\sin \theta} \right) L_y r^2 = f(\theta) L_y r^2 \quad (3)$$

$$A_{LV} = \frac{2\theta}{\sin \theta} L_y r \quad (4)$$

$$A_{SL} = 2L_y r \quad (5)$$

where $f(\theta) = \frac{\theta}{\sin^2 \theta} - \frac{\cos \theta}{\sin \theta}$, θ is the contact angle, r is the contact radius, and L_y is the length of the cylindrical drop in the y direction. Therefore, for a droplet at a constant volume, we have

$$\frac{d\theta}{dr} = \frac{\sin \theta (\theta - \sin \theta \cos \theta)}{r (\theta \cos \theta - \sin \theta)} \quad (6)$$

The important contributions to the Gibbs free energy of the cylindrical drop come from the interfacial terms

$$G = \gamma_{LV} A_{LV} + (\gamma_{SL} - \gamma_{SV}) A_{SL} = 2 \left(\frac{\theta}{\sin \theta} - \cos \theta \right) \gamma_{LV} L_y r \quad (7)$$

where γ_{LV} , γ_{SL} , and γ_{SV} are the liquid–gas, solid–liquid, and solid–gas surface tensions, respectively. The term involving γ_{SL} and γ_{SV} is simplified using Young's equation for the equilibrium contact angle θ_0 . It is noticed here that θ_0 and r_0 are supposed to be the droplet's contact angle and radius at the equilibrium state, respectively. The corresponding contact angle and radius at the nonequilibrium state are $\theta = \theta_0 - \delta\theta$ and $r = r_0 + \delta r$, respectively. Using eqs 6 and 7 and the Taylor expansion, the following equation is obtained

$$\delta G = G(r) - G(r_0) \approx \frac{\sin \theta_0 - \theta_0 \cos \theta_0}{\theta_0 - \sin \theta_0 \cos \theta_0} (\delta\theta)^2 \gamma_{LV} L_y r \quad (8)$$

where δG is the excess Gibbs free energy of the nonequilibrium droplet, compared to the equilibrium state. Here, the Gibbs free energy (G) and excess Gibbs free energy (δG) are normalized by $2\gamma_{LV}\sqrt{VL_y}$, i.e.,

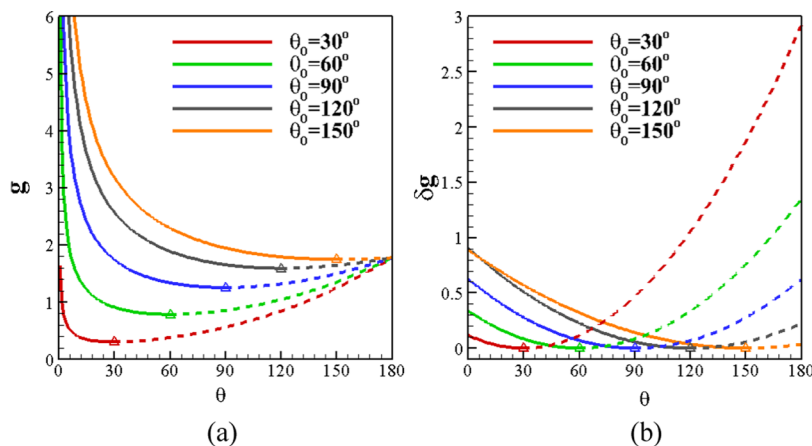


Figure 7. (a) Normalized Gibbs free energy and (b) normalized excess Gibbs free energy as functions of θ . The equilibrium contact angle θ_0 increases from 30 to 150° with a 30° increment. The triangles in (a) and (b) denote the points where $\frac{dG}{d\theta} = 0$ and $\frac{d(\delta G)}{d\theta} = 0$. The solid lines represent the physical evaporation process, in which θ is always smaller than θ_0 .

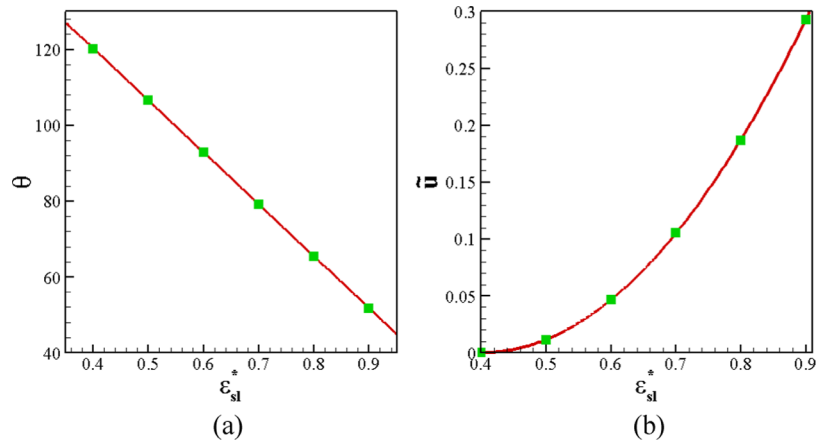


Figure 8. (a) Contact angle (θ) as a function of the liquid–solid interaction (ϵ_{sl}^*). (b) Intrinsic energy barrier (\bar{u}) as a function of the liquid–solid interaction (ϵ_{sl}^*) when the equilibrium contact angle $\theta_0 = \theta_H = 119^\circ$.

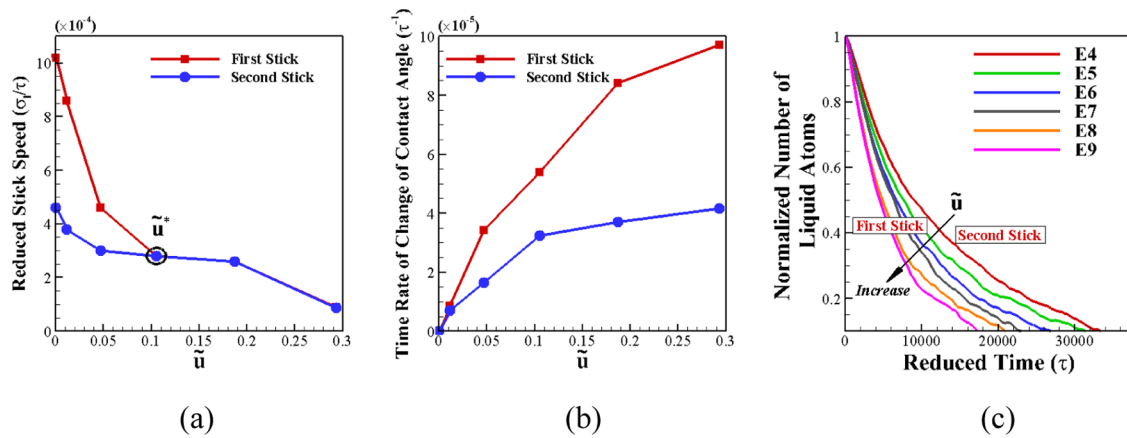


Figure 9. (a) First stick speed u_{s1} and the second stick speed u_{s2} as functions of intrinsic energy barrier (\bar{u}). (b) Time rate of change of contact angles u_{c1} and u_{c2} in the first and second stick period, respectively as functions of (\bar{u}). (c) Normalized number of liquid atoms as a function of time. The direction of the arrow in the figure indicates the increase of the intrinsic energy barrier, and the left and right sides of the arrow approximately represent the first and second stick processes. For comparison, all parameters have been normalized by their initial values.

$$g = \frac{G}{2\gamma_{LV}\sqrt{VL_y}} = \frac{\theta - \sin \theta \cos \theta_0}{\sqrt{\theta - \sin \theta \cos \theta}} \quad (9)$$

$$\delta g = \frac{\delta G}{2\gamma_{LV}\sqrt{VL_y}} = \frac{\sin \theta_0 (\sin \theta_0 - \theta_0 \cos \theta_0) (\delta \theta)^2}{(\theta_0 - \sin \theta_0 \cos \theta_0)^{3/2} \cdot 2} \quad (10)$$

From eqs 9 and 10, we can see that the normalized Gibbs free energy (g) and normalized excess Gibbs free energy (δg) are functions of θ_0 and θ . g and δg as functions of θ for a specific θ_0 are shown in Figure 7a,b, respectively. In the evaporation process, θ is always smaller than θ_0 and therefore $\delta\theta = \theta_0 - \theta$ is always positive. Hence, only the solid lines in the region $\theta < \theta_0$ in Figure 7a,b represent a physical process. Figure 7a shows that for a specific θ_0 , as θ increases, g decreases first and then increases a little bit. Since θ_0 corresponds to the equilibrium contact angle, of course, we have $[dg/d\theta]_{\theta=\theta_0} = 0$ in Figure 7a. Figure 7b shows δg as a quadratic function of θ ($\delta\theta = \theta_0 - \theta$). For a specific θ_0 , at the equilibrium state with $\theta = \theta_0$, we have $\delta g = 0$.

In our descriptions, $\theta_0 = \theta_H$, and at $\theta = \theta_L$ the corresponding δg is exactly the intrinsic energy barrier of the system \bar{u} , which is related only to the neighboring stripes' fluid–solid interactions. In the evaporation process, when $\delta g > \bar{u}$, there is sufficient

energy available to overcome the hysteresis barrier effect and the contact line would jump to its next equilibrium position with $\theta = \theta_H$.

To explore the relationship between stick speed and intrinsic energy barrier, we fix stripe A with E4 ($\epsilon_{sl}^* = 0.4$ and corresponding $\theta_H = 119^\circ$) and set stripe B's fluid–solid interaction strength from E4 to E9. In the cases with E5, E6, ..., E9, the corresponding $\theta_L < \theta_H$. Different solid–liquid interaction strengths (ϵ_{sl}^*) would result in different contact angles. First, the wetting characteristics of a droplet on a homogeneous substrate with a specified ϵ_{sl}^* can be obtained through simulations. The obtained equilibrium contact angle θ as a function of ϵ_{sl}^* is shown in Figure 8a. It is seen that θ decreases linearly with ϵ_{sl}^* . Second, from Figure 8a, a specified ϵ_{sl}^* of stripe B, for example, $\epsilon_{sl}^* = 0.5$, would lead to an equilibrium contact angle, which corresponds to θ_L in our further simulation of d6 heterogeneous system. Then, $\delta\theta = \theta_H - \theta_L$ can be obtained. Using $\delta\theta$ and $\theta_0 = \theta_H$, δg , i.e., \bar{u} can be calculated from eq 10. In this way, the intrinsic energy barrier of the system \bar{u} as a function of ϵ_{sl}^* can be obtained, which is shown in Figure 8b. It is seen that the stronger the stripe B's hydrophilicity the larger the intrinsic energy barrier.

The stick speeds of the two "stick" processes obtained from our simulations are shown in Figure 4b. The two stick processes

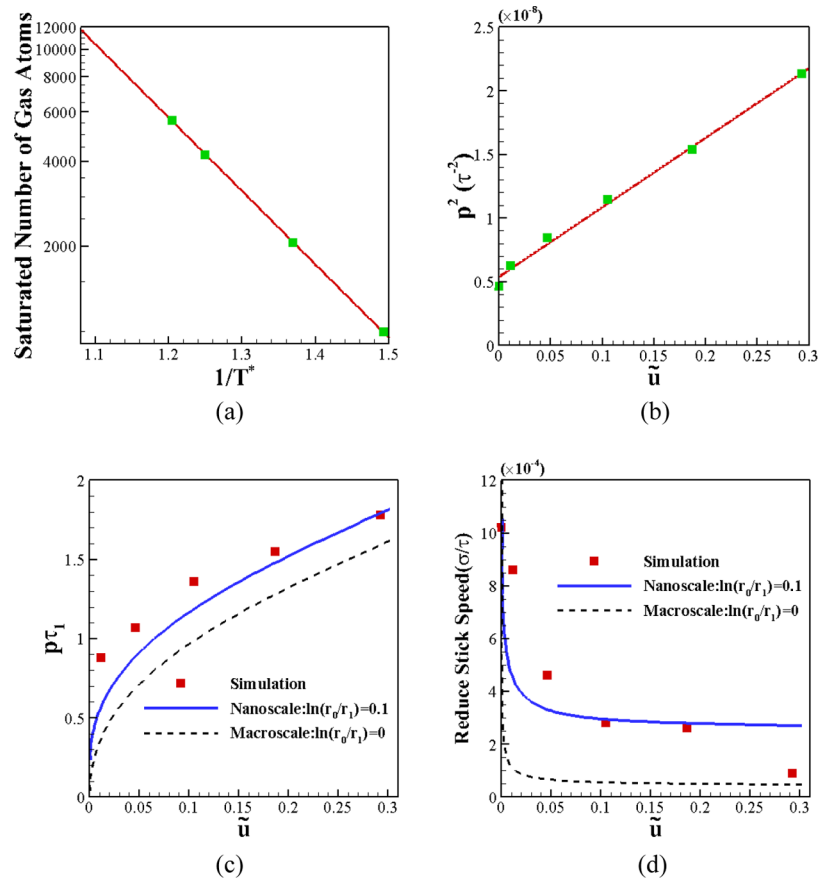


Figure 10. (a) Saturated number of gas atoms as a function of the substrate's temperature when the system is in equilibrium. (b) Attenuation index p^2 as a function of intrinsic energy barrier (\tilde{u}) when $\theta_H = 119^\circ$. (c) $p\tau_1$ as a function of intrinsic energy barrier (\tilde{u}) when $\theta_H = 119^\circ$. (d) The first stick speed u_{s1} as a function of intrinsic energy barrier (\tilde{u}) when $\theta_H = 119^\circ$. The scattered points are simulation results, and the lines in (c) and (d) are analytical predictions.

during τ_1 and τ_3 are referred to as the “first stick” and “second stick” (see Figure 6). The first and second stick speeds u_{s1} and u_{s2} , respectively, as functions of \tilde{u} are shown in Figure 9a. When both stripes' strength is $E4$, it actually represents a homogeneous substrate and the evaporation mode is CCA. From Figure 5a, we have seen usually for the heterogeneous cases there is a very short jump period τ_2 between the first stick [the period τ_1 , i.e., $t \in (0, 13\,600)\tau$] and the second stick [the period τ_3 , i.e., $t \in (14\,500, 26\,000)\tau$]. For the homogeneous case, the jump process would disappear ($\tau_2 = 0$). However, to compare with heterogeneous cases, we artificially divide the homogeneous evaporation process ($t \approx 30\,000\tau$) into two stick processes with equal periods, i.e., $\tau_1 = \tau_3 \approx 15\,000\tau$. For this homogeneous case, the speeds of its contact line u_{s1} and u_{s2} actually mean slip speeds during the two artificial stick processes (see Figure 9c).

From Figure 9a, we can see that as \tilde{u} increases u_{s1} and u_{s2} initially decrease rapidly and then slow down. Generally speaking, the contact line's moving speed decreases with increasing \tilde{u} . This is due to the fact that \tilde{u} indicates the restriction strength of the heterogeneous substrate to the contact line. Actually, the stick speed is basically in the magnitude of about 10^{-2} m/s in dimension for a nanodroplet, which is a relatively large value on the macroscopic scale. That may be due to the scaling effect.⁴⁵ In the following text, first we would like to theoretically explain why the contact line's moving speed decreases with \tilde{u} increasing.

The number of liquid phase particles in our simulation is exponentially decayed over time, i.e.,

$$N_L = N_0 e^{-pt} \quad (11)$$

where N_0 is the initial number of liquid atoms before the temperature of the substrate increases and $p > 0$ is related to the contact angle θ . A detailed derivation of eq 11 is given in Appendix A. When the substrate is homogeneous, we have $p \propto \theta$. For the heterogeneous substrate, $p \propto (\theta_H - \theta)$ and $\tilde{u} \propto (\theta_H - \theta)^2$ (in this study, $\theta_H = 119^\circ$). Hence, we can obtain $p^2 \propto \tilde{u}$. The attenuation index p^2 as a function of the intrinsic energy barrier \tilde{u} , i.e., $p^2 = h(\tilde{u})$ is shown in Figure 10b. Using eqs 3 and 11, and ignoring the change of the density during evaporation, we can obtain

$$p\tau_1 = \ln \frac{f(\theta_H)}{f(\theta_L)} + 2\ln \frac{r_0}{r_1} \quad (12)$$

$$\begin{aligned} u_{s1} &= 2 \frac{r|_{t=0} - r|_{t=\tau_1}}{\tau_1} \\ &= \frac{2}{p\tau_1} \left(\frac{N_0}{\rho Ly} \right)^{1/2} (f^{-1/2}(\theta_H) - f^{-1/2}(\theta_L) e^{-1/2p\tau_1}) h^{1/2}(\tilde{u}) \end{aligned} \quad (13)$$

where $r_0 = L_0/2$ and $r_1 = L_1/2$. The second term $\left(2\ln \frac{r_0}{r_1} \right)$ on the right-hand side of eq 12 indicates the scale effect. At the

macroscale, the term $\ln \frac{r_0}{r_1}$ is very close to zero ($\frac{r_0}{r_1} \approx 1$) and can be ignored because $r_0 - r_1 \leq 7\sigma_1$ and usually $r_0 > 10^3\sigma_1$.⁴³ However, at the nanoscale, the term $\left(\ln \frac{r_0}{r_1}\right)$ is on the order of 10^{-1} in our simulations; therefore, for simplicity $\ln \frac{r_0}{r_1} = 0.1$ is adopted in the analytical prediction. $p\tau_1$ and u_{s1} as functions of intrinsic energy barrier \tilde{u} are shown in Figure 10c,10d, respectively. The dashed line in Figure 10d shows that the stick speed decreases dramatically approximately from $10 \times 10^{-4}\sigma_1/\tau$ to $1 \times 10^{-4}\sigma_1/\tau$, which is close to 0. Hence, it is reasonable to assume that the contact line is completely stationary in the macro CCR model. However, at the nanoscale, it is seen that the stick speed decreases more slowly. The analytical prediction at the nanoscale qualitatively agrees well with the simulation result.

From Figure 9a, we also found that the first stick speed u_{s1} is generally larger than the second stick speed u_{s2} at a small \tilde{u} . For example, at $\tilde{u} = 0$, u_{s1} and u_{s2} are approximately $10.2 \times 10^{-4}\sigma_1/\tau$ and $4.6 \times 10^{-4}\sigma_1/\tau$, respectively. When the substrate is homogeneous, using eqs 3 and 11, and ignoring the change of the density during evaporation, we have the evaporation rate $-\frac{dN_L}{dt}$ and the stick speed u_s as

$$-\frac{dN_L}{dt} = pN_0 e^{-p\tilde{u}} \quad (14)$$

$$u_s = -\frac{2dr}{dt} = p \left(\frac{N_0 \sin^2 \theta e^{-p\tilde{u}}}{\rho L_y (\theta - \sin \theta \cos \theta)} \right)^{1/2} \quad (15)$$

Furthermore, we get u_s as a function of the evaporation rate and contact angle

$$u_s = \left(\frac{p \sin^2 \theta}{\rho L_y (\theta - \sin \theta \cos \theta)} \right)^{1/2} \left(-\frac{dN_L}{dt} \right)^{1/2} \quad (16)$$

When the substrate is homogeneous (θ is a constant), u_s is only a function of evaporation rate $-\frac{dN_L}{dt}$. Furthermore, the larger the evaporation rate, the faster the contact line moves. However, when the substrate is heterogeneous, the contact angle θ may also change during droplet evaporation. u_s depends on $\frac{d\theta}{dt}$ and $-\frac{dN_L}{dt}$ simultaneously. Our results show that the difference between the first stick and the second stick will be smaller when \tilde{u} becomes larger. From Figure 9a,c, we can see that when $\tilde{u} > \tilde{u}^*$, where $\tilde{u}^* \approx 0.11$, $u_{s1} \approx u_{s2}$ although the evaporation rates at the first stick and the second stick are different. That may suggest that the moving speed of the contact line when the droplet evaporates from the same heterogeneous surface at the same temperature T^* is no longer relevant to the evaporation rate when $\tilde{u} > \tilde{u}^*$.

The time rate of change of contact angle u_{c1} and u_{c2} as functions of \tilde{u} are shown in Figure 9b. It is seen that u_{c1} and u_{c2} generally increase with increasing \tilde{u} . The larger the intrinsic energy barrier, the faster the contact angle changes. The possible reason is that at the nanometer scale, as the stripe B becomes more hydrophilic (\tilde{u} increases), the evaporation rate becomes faster (see Figure 9c). Because the contact line's moving speed is slower as \tilde{u} increases, to match the faster evaporation rate, the time rate of change of contact angle correspondingly becomes larger.

SUMMARY AND CONCLUSIONS

The evaporation of a cylindrical nanodroplet consisting of Lennard-Jones particles from heterogeneous surfaces was studied by molecular dynamics simulations. The surface consists of alternating stripes of equal width but two chemical types, which lead to different contact angles.

First, we studied the evaporation patterns of the d6 system. Besides, our results confirmed that pinning is a dynamic process with a slow movement of the contact lines from the nanoscale point of view.

Second, we studied the thermal effect on the shape of the droplet during the evaporation process. The thermal effect can be decomposed into three factors: volume expansion, local evaporation near the three-phase contact line, and nonuniform evaporation. The whole evaporation process is found to be generally dominated by the nonuniform evaporation, and the time span of the effect is approximately $10^4\tau$. The volume expansion and local evaporation effects only play important roles at the initial moment. Also, the time span of their impact is 1 to 2 orders of magnitude lower than that of the nonuniform evaporation effect.

Finally, we used the stick-jump evaporation mode at the nanoscale to explore the dynamics and mechanism of pinning. From the nanoscale point of view, the slow movement of the contact line during the pinning process is observed. Our results show that the stick speed may be influenced by the intrinsic energy barrier \tilde{u} and the evaporation rate. Generally speaking, the larger the intrinsic energy barrier, the slower the contact line moves. When the contact line moves slower, the contact angle changes faster.

At the specified temperature, when $\tilde{u} < \tilde{u}^*$, where \tilde{u}^* is the critical energy barrier, the speed of the contact line would decrease with the decreasing evaporate rate. Since the evaporation rate decays exponentially during evaporation, the speed of the second stick is generally smaller than that of the first stick. However, when $\tilde{u} > \tilde{u}^*$, the contact line speed is no longer relevant to the evaporation rate at different stages (the first stick and the second stick).

APPENDIX A

Based on the diffusion equation^{11,12,46}

$$\frac{d(N_L m)}{dt} = \frac{dM_L}{dt} = -D \int \nabla c \, dS \quad (17)$$

where m and M_L are the mass of a liquid atom and the mass of the liquid phase, respectively; t is the evaporation time; N_L is the number of the liquid-phase atoms; D is the diffusion coefficient of the vapor; c is the vapor concentration; and S is the surface of the liquid phase. It is seen that the droplet evaporation rate is proportional to the concentration difference. Then, we have

$$\frac{dN_L}{dt} \propto \nabla c \propto (c_{T91} - c_0) \quad (18)$$

with

$$c_{T91} = \frac{N_{\text{sat}_T91}}{V_{\text{vap}_T91}}, \quad c_0 = \frac{N_g}{V_{\text{vap}}} = \frac{N_T - N_L}{V_{\text{vap}}} \quad (19)$$

where c_{T91} , N_{sat_T91} , and V_{vap_T91} are the saturated vapor concentration, the saturated number of the vapor-phase atoms, and the volume of the vapor phase, respectively, when the system is at the equilibrium state ($T^* = 0.91$). c_0 , N_g , and V_{vap} are

the vapor concentration, the number of the vapor-phase atoms, and the volume of the vapor phase during evaporation, respectively, and the N_T is the total number of the vapor- and liquid-phase atoms. Ignoring the change of the volume of the vapor phase during evaporation and $V_{\text{vap}} \approx V_{\text{vap}_T}$, we have

$$\frac{dN_L}{dt} = -p[N_{\text{sat}_T} - (N_T - N_L)] \quad (20)$$

$$N_L|_{t=0} = N_T - N_{\text{sat}_T}, \quad N_L|_{t=\infty} = N_T - N_{\text{sat}_T} \quad (21)$$

where p is the attenuation index and $p > 0$ and N_{sat_T} is the saturated number of the vapor-phase atoms when $T^* = 0.67$. Equation 21 shows the initial ($t = 0$) and final ($t = \infty$) conditions. The solution of the ordinary differential equation eq 20 is

$$N_L = (N_T - N_{\text{sat}_T}) + (N_{\text{sat}_T} - N_{\text{sat}_T}) e^{-pt} \quad (22)$$

The number of the saturated vapor-phase atoms is a function of the temperature⁴⁷

$$\lg N_{\text{sat}} = \frac{-B}{T^*} + E \quad (23)$$

where N_{sat} is the saturated number of the vapor-phase atoms and B and E are constants. The saturate number of the vapor-phase atoms as a function of the substrate's temperature at an equilibrium state is shown in Figure 10a. From Figure 10a, it is seen that when the substrate's temperature is 0.91 the saturated number of the vapor-phase atoms is approximately 11 115, which is the sum of the number of the liquid-vapor atoms in our simulations ($N_{\text{sat}_T} \approx N_T$) and $N_T - N_{\text{sat}_T} \ll N_{\text{sat}_T} - N_{\text{sat}_T}$. Thus, the solution of eq 20 can be written

$$N_L = N_0 e^{-pt} \quad (24)$$

where $N_0 \approx N_{\text{sat}_T} - N_{\text{sat}_T}$ is the initial number of the liquid atoms at $t = 0$.

AUTHOR INFORMATION

Corresponding Author

*E-mail: huanghb@ustc.edu.cn.

ORCID

Haibo Huang: 0000-0002-1308-9900

Notes

The authors declare no competing financial interest.

ACKNOWLEDGMENTS

This work was supported by the Natural Science Foundation of China (NSFC) Grant Nos. 11872064 and 11621202. H.H. is supported by NSFC Grant No. 11472269.

REFERENCES

- (1) Park, J.; Moon, J. Control of colloidal particle deposit patterns within picoliter droplets ejected by ink-jet printing. *Langmuir* **2006**, *22*, 3506–3513.
- (2) Jing, J.; Reed, J.; Huang, J.; Hu, X.; Clarke, V.; Edington, J.; Housman, D.; Anantharaman, T. S.; Huff, E. J.; Mishra, B. Automated high resolution optical mapping using arrayed, fluid-fixed DNA molecules. *Proc. Natl. Acad. Sci. U.S.A.* **1998**, *95*, 8046–8051.
- (3) Hsieh, C.-C.; Li, L.; Larson, R. G. Modeling hydrodynamic interaction in Brownian dynamics: simulations of extensional flows of dilute solutions of DNA and polystyrene. *J. Non-Newtonian Fluid Mech.* **2003**, *113*, 147–191.

(4) Xia, D.; Brueck, S. A facile approach to directed assembly of patterns of nanoparticles using interference lithography and spin coating. *Nano Lett.* **2004**, *4*, 1295–1299.

(5) Bigioni, T. P.; Lin, X.-M.; Nguyen, T. T.; Corwin, E. I.; Witten, T. A.; Jaeger, H. M. Kinetically driven self assembly of highly ordered nanoparticle monolayers. *Nat. Mater.* **2006**, *5*, 265.

(6) Deegan, R. D.; Bakajin, O.; Dupont, T. F.; Huber, G.; Nagel, S. R.; Witten, T. A. Capillary flow as the cause of ring stains from dried liquid drops. *Nature* **1997**, *389*, 827.

(7) Deegan, R. D.; Bakajin, O.; Dupont, T. F.; Huber, G.; Nagel, S. R.; Witten, T. A. Contact line deposits in an evaporating drop. *Phys. Rev. E* **2000**, *62*, 756.

(8) Birdi, K. S.; Vu, D. T.; Winter, A. A study of the evaporation rates of small water drops placed on a solid surface. *J. Phys. Chem.* **1989**, *93*, 3702–3703.

(9) Erbil, H. Y.; McHale, G.; Newton, M. I. Drop evaporation on solid surfaces: constant contact angle mode. *Langmuir* **2002**, *18*, 2636–2641.

(10) Hu, H.; Larson, R. G. Evaporation of a sessile droplet on a substrate. *J. Phys. Chem. B* **2002**, *106*, 1334–1344.

(11) Xu, W.; Leeladhar, R.; Kang, Y. T.; Choi, C.-H. Evaporation kinetics of sessile water droplets on micropillared superhydrophobic surfaces. *Langmuir* **2013**, *29*, 6032–6041.

(12) Rowan, S. M.; Newton, M. I.; McHale, G. Evaporation of microdroplets and the wetting of solid surfaces. *J. Phys. Chem.* **1995**, *99*, 13268–13271.

(13) Ristenpart, W. D.; Kim, P. G.; Domingues, C.; Wan, J.; Stone, H. Influence of substrate conductivity on circulation reversal in evaporating drops. *Phys. Rev. Lett.* **2007**, *99*, No. 234502.

(14) Hu, H.; Larson, R. G. Analysis of the microfluid flow in an evaporating sessile droplet. *Langmuir* **2005**, *21*, 3963–3971.

(15) Zhang, J.; Leroy, F.; Müller-Plathe, F. Evaporation of nanodroplets on heated substrates: a molecular dynamics simulation study. *Langmuir* **2013**, *29*, 9770–9782.

(16) Zhang, J.; Leroy, F.; Müller-Plathe, F. Influence of contact-line curvature on the evaporation of nanodroplets from solid substrates. *Phys. Rev. Lett.* **2014**, *113*, No. 046101.

(17) Orejon, D.; Sefiane, K.; Shanahan, M. E. R. Stick-slip of evaporating droplets: substrate hydrophobicity and nanoparticle concentration. *Langmuir* **2011**, *27*, 12834–12843.

(18) Moffat, J. R.; Sefiane, K.; Shanahan, M. E. R. Effect of TiO₂ nanoparticles on contact line stick-slip behavior of volatile drops. *J. Phys. Chem. B* **2009**, *113*, 8860–8866.

(19) Chen, X.; Ma, R.; Li, J.; Hao, C.; Guo, W.; Luk, B. L.; Li, S. C.; Yao, S.; Wang, Z. Evaporation of droplets on superhydrophobic surfaces: Surface roughness and small droplet size effects. *Phys. Rev. Lett.* **2012**, *109*, No. 116101.

(20) Li, Q.; Zhou, P.; Yan, H. J. Pinning-depinning mechanism of the contact line during evaporation on chemically patterned surfaces: a lattice Boltzmann study. *Langmuir* **2016**, *32*, 9389–9396.

(21) Xu, W.; Choi, C.-H. Effects of surface topography and colloid particles on the evaporation kinetics of sessile droplets on superhydrophobic surfaces. *J. Heat Transfer* **2012**, *134*, No. 051022.

(22) Maxwell, J. C. *The Scientific Papers of James Clerk Maxwell*; University Press, 1890; Vol. 2.

(23) Malvadkar, N. A.; Hancock, M. J.; Sekeroglu, K.; Dressick, W. J.; Demirel, M. C. An engineered anisotropic nanofilm with unidirectional wetting properties. *Nat. Mater.* **2010**, *9*, 1023.

(24) Leroy, F.; Müller-Plathe, F. Can continuum thermodynamics characterize wenzel wetting states of water at the nanometer scale? *J. Chem. Theory Comput.* **2012**, *8*, 3724–3732.

(25) Leroy, F.; Müller-Plathe, F. Rationalization of the behavior of solid-liquid surface free energy of water in Cassie and Wenzel wetting states on rugged solid surfaces at the nanometer scale. *Langmuir* **2011**, *27*, 637–645.

(26) Forsberg, P. S. H.; Priest, C.; Brinkmann, M.; Sedev, R.; Ralston, J. Contact line pinning on microstructured surfaces for liquids in the Wenzel state. *Langmuir* **2010**, *26*, 860–865.

- (27) Papadopoulos, P.; Mammen, L.; Deng, X.; Vollmer, D.; Butt, H.-J. How superhydrophobicity breaks down. *Proc. Natl. Acad. Sci. U.S.A.* **2013**, *110*, 3254–3258.
- (28) Extrand, C. W. Contact angles and hysteresis on surfaces with chemically heterogeneous islands. *Langmuir* **2003**, *19*, 3793–3796.
- (29) Matsui, H.; Noda, Y.; Hasegawa, T. Hybrid energy-minimization simulation of equilibrium droplet shapes on hydrophilic/hydrophobic patterned surfaces. *Langmuir* **2012**, *28*, 15450–15453.
- (30) Jansen, H. P.; Bliznyuk, O.; Kooij, E. S.; Poelsema, B.; Zandvliet, H. J. Simulating anisotropic droplet shapes on chemically striped patterned surfaces. *Langmuir* **2012**, *28*, 499–505.
- (31) Varagnolo, S.; Ferraro, D.; Fantinel, P.; Pierno, M.; Mistura, G.; Amati, G.; Biferale, L.; Sbragaglia, M. Stick-slip sliding of water drops on chemically heterogeneous surfaces. *Phys. Rev. Lett.* **2013**, *111*, No. 066101.
- (32) Chu, K. H.; Xiao, R.; Wang, E. N. Uni-directional liquid spreading on asymmetric nanostructured surfaces. *Nat. Mater.* **2010**, *9*, 413.
- (33) Kusumaatmaja, H.; Yeomans, J. M. Modeling contact angle hysteresis on chemically patterned and superhydrophobic surfaces. *Langmuir* **2007**, *23*, 6019–6032.
- (34) Kusumaatmaja, H.; Yeomans, J. M. Controlling drop size and polydispersity using chemically patterned surfaces. *Langmuir* **2007**, *23*, 956–959.
- (35) Wang, F.-C.; Wu, H.-A. Pinning and depinning mechanism of the contact line during evaporation of nano-droplets sessile on textured surfaces. *Soft Matter* **2013**, *9*, 5703–5709.
- (36) Jansen, H. P.; Zandvliet, H. J. W.; Kooij, E. S. Evaporation of elongated droplets on chemically stripe-patterned surfaces. *Int. J. Heat Mass Transf.* **2015**, *82*, 537–544.
- (37) Maheshwari, S.; van der Hoef, M.; Zhang, X.; Lohse, D. Stability of surface nanobubbles: A molecular dynamics study. *Langmuir* **2016**, *32*, 11116–11122.
- (38) Lohse, D.; Zhang, X. Surface nanobubbles and nanodroplets. *Rev. Mod. Phys.* **2015**, *87*, 981.
- (39) Wang, F.-C.; Wu, H.-A. Molecular origin of contact line stick-slip motion during droplet evaporation. *Sci. Rep.* **2015**, *5*, No. 17521.
- (40) Mazloomi Moqaddam, A.; Derome, D.; Carmeliet, J. Dynamics of Contact Line Pinning and Depinning of Droplets Evaporating on Microribs. *Langmuir* **2018**, *34*, 5635–5645.
- (41) Xu, W.; Choi, C. H. From sticky to slippery droplets: dynamics of contact line depinning on superhydrophobic surfaces. *Phys. Rev. Lett.* **2012**, *109*, No. 024504.
- (42) Shanahan, M. E. R. Simple theory of “stick-slip” wetting hysteresis. *Langmuir* **1995**, *11*, 1041–1043.
- (43) Zhang, J.; Müller-Plathe, F.; Leroy, F. Pinning of the contact line during evaporation on heterogeneous surfaces: slowdown or temporary immobilization? Insights from a nanoscale study. *Langmuir* **2015**, *31*, 7544–7552.
- (44) Plimpton, S. Fast parallel algorithms for short-range molecular dynamics. *J. Comput. Phys.* **1995**, *117*, 1–19.
- (45) Lv, C.; Chen, C.; Chuang, Y.-C.; Tseng, F.-G.; Yin, Y.; Grey, F.; Zheng, Q. Substrate curvature gradient drives rapid droplet motion. *Phys. Rev. Lett.* **2014**, *113*, No. 026101.
- (46) Erbil, H. Y. Evaporation of pure liquid sessile and spherical suspended drops: A review. *Adv. Colloid Interface Sci.* **2012**, *170*, 67–86.
- (47) Koutsoyiannis, D. Clausius–Clapeyron equation and saturation vapour pressure: simple theory reconciled with practice. *Eur. J. Phys.* **2012**, *33*, 295.